

Remarkable Activity of 002 Facet of Ruthenium Nanoparticles Grown on Graphene Films on the Photocatalytic CO₂ Methanation

Aicha Anouar, Rocío García-Aboal, Pedro Atienzar, Antonio Franconetti, Nadia Katir, Abdelkrim El Kadib, Ana Primo,* and Hermenegildo Garcia*

In the context of diminishing atmospheric CO₂ emissions, there is an urgent need to develop processes that can be carried out at a scale commensurate with appropriate CO₂ volumes. One possible reaction is the transformation of CO₂ to methane (Sabatier reaction). Due to its chemical stability, catalytic CO₂ hydrogenation to methane is carried out at temperatures of 450 °C or higher and pressures above 5 bars, thus, requiring a significant energy input. One alternative possibility to conventional thermal catalysis is the use of solar light as the primary energy, performing the photocatalytic CO₂ hydrogenation. In this broad context, the present study shows the photocatalytic activity of nanometric films of oriented Ru nanoparticles (NPs) strongly grafted on defective graphene. These graphene films (thinner than 20 nm) containing Ru NPs nanoplatelets (less than 2 nanomol_{Ru}/cm²) are among the most active photocatalysts ever prepared for CO₂ hydrogenation and operate through photoinduced charge separation.

feedstock for the production of fuels and chemicals.^[2,3]

Although the majority of the reactions involving CO₂ as reagent are thermodynamically uphill, hydrogenations to effect the chemical reduction of CO₂ are among the few exothermic processes.^[4,5] CO₂ hydrogenations can be carried out by conventional thermal catalysis, but recently the photocatalytic version of CO₂ hydrogenation has gained importance due to the possibility to use solar light as the only energy source.^[6–9] Among the different photocatalysts that have been reported to promote CO₂ hydrogenation, those containing ruthenium or ruthenium oxide nanoparticles (NPs) in combination with a semiconductor exhibit a high activity.^[10–15] Pre-

vious studies have shown that graphene or graphitic carbon nitride in combination with metal NPs is a suitable photocatalyst for the light-assisted Sabatier CO₂ hydrogenation to methane.^[16–19]

In the present study, we report the specific photocatalytic activity for CO₂ hydrogenation corresponding to two facet-oriented Ru NPs exhibiting preferential crystallographic planes grafted on defective graphene. Optimization of the catalytic performance of metal NPs is an issue of constant interest in heterogeneous catalysis.^[20] One possibility to achieve this goal is to prepare samples of metal NPs exposing the most active crystallographic plane,^[21–23] which prospectively requires to set a facet-activity relationship. While theoretical studies predict that different planes in a crystal should exhibit different activities,^[24] the main problem is how to provide experimental confirmation of these theoretical predictions and how to prepare reliably samples exhibiting defined preferential orientations of the crystal.^[25–27] The case of Ru metal is particularly interesting given its high activity as a catalyst in many reactions, while being elusive to undergo preferential facet orientation.^[16]

One of the most general methodologies to grow crystals with preferential orientation is the use of complexing agents that by strong binding with certain crystal planes thwart their growth during the formation of the crystals.^[28,29] Fluoride and ionic surfactants are typical complexing agents widely used in this methodology.^[30–33] These surface complexing agents may remain attached to the surface after preparation of the sample, thus, hindering full accessibility to the exposed catalytic


1. Introduction

Due to the current concerns on global warming, there is an international consensus in diminishing atmospheric CO₂ emissions.^[1] While the goal of a totally decarbonized society would require the shift from fossil fuels to renewable energies, one possibility to decrease CO₂ emissions is to use this gas as

A. Anouar, R. García-Aboal, P. Atienzar, A. Primo, H. Garcia
 Instituto Universitario de Tecnología Química CSIC-UPV
 Universitat Politècnica de València
 Av. De los Naranjos s/n, Valencia 46022, Spain
 E-mail: aprimoar@qim.upv.es; hgarcia@qim.upv.es

A. Anouar, N. Katir, A. E. Kadib
 Euromed Research Center
 Engineering Division
 Euro-Med University of Fès (UEMF)
 Route de Meknes, Rond-point de Bensouda, Fès 30070, Morocco

A. Franconetti
 Departamento Química Orgánica
 Facultad de Química
 Universidad de Sevilla
 Profesor García Gonzalez 1, Sevilla 41012, Spain

 The ORCID identification number(s) for the author(s) of this article can be found under <https://doi.org/10.1002/adsu.202100487>.

© 2022 The Authors. Advanced Sustainable Systems published by Wiley-VCH GmbH. This is an open access article under the terms of the Creative Commons Attribution-NonCommercial License, which permits use, distribution and reproduction in any medium, provided the original work is properly cited and is not used for commercial purposes.

DOI: 10.1002/adsu.202100487

Alternatively, crystals are grown on substrates exhibiting specific facets that favor the epitaxial growth of planes matching the templating substrate surface.^[34,35] This approach has the main drawback of the limited choice of available substrate library with clean surface to promote the growth of the nascent NPs.

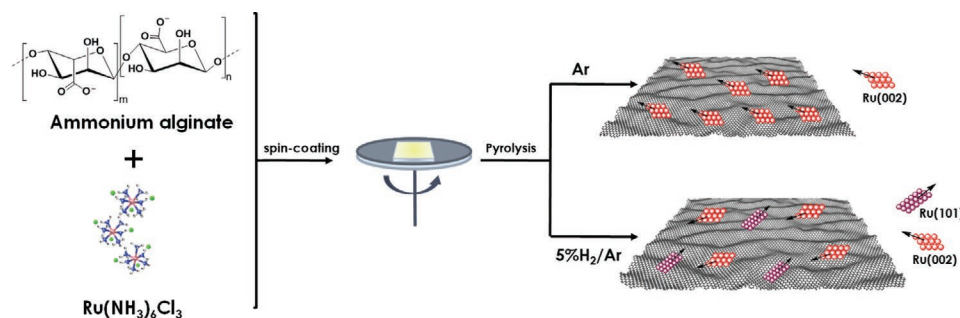
In this context, we have previously reported that pyrolysis of films of natural polysaccharides containing adsorbed metal salts may afford metal NPs exhibiting a defined preferential crystallographic orientation.^[36–42] After thermal annealing that converts these raw polysaccharides into few-layers graphene, the resulting metal NPs grow anisotropically on the defective graphene basal plane, without the interference of complexing agents.

Following this methodology, herein we report the preparation of films of Ru NPs grafted on graphene with two defined facets orientation, either 002 ($\overline{Ru}(002)/G$) or 002 and 101 ($\overline{Ru}(002-101)/G$). Activity data for photocatalytic CO₂ methanation clearly showed that 002 facet is far more active to promote the photocatalytic CO₂ methanation compared to the 101 plane. Theoretical calculations at DFT level suggest that this high activity derives from the lower adsorption energy of H₂ on the 002 plane as compared to the stronger hydrogen chemisorption on the 101 facet. The present results show the remarkable activity increase that can be achieved also in photocatalysis by preparing metal NPs exposing the most active plane to interact with substrates and reagents.

2. Results and Discussion

2.1. Photocatalyst Characterization

The photocatalysts of the present study were thin films of nanometric thickness constituted by multi-layers defective graphene containing Ru NPs. The preparation procedure of these films is illustrated in **Scheme 1**. The process uses an aqueous solution of ammonium alginate at neutral pH followed by which hexaammineruthenium(III) chloride is added. A clear brown solution suitable for casting obtained after filtration of the metallic suspension is spin-coated onto freshly cleaned quartz plates. Pyrolysis at 1000 °C of these films produces the transformation of ammonium alginate into multilayers graphene on top of which the presence of Ru NPs was observed. Depending on the atmosphere of pyrolysis used, Ar or 5% H₂/Ar, $\overline{Ru}(002)/G$, or $\overline{Ru}(002-101)/G$ films are formed. As it will be



Scheme 1. Pictorial illustration of the preparation of $\overline{Ru}(002)/G$ and $\overline{Ru}(002-101)/G$ films.

Table 1. Characterization data of facet-oriented Ru films.

Sample	Ru loading [mol cm ⁻²] ^{a)}	Average NP height [nm] ^{b)}	Film thickness [nm] ^{b)}
$\overline{Ru}(002)/G$	1.34·10 ⁻⁹	4.3 ± 0.2	13.3 ± 0.3
$\overline{Ru}(002-101)/G$	1.76·10 ⁻⁹	7.6 ± 0.3	19.5 ± 0.4

^{a)} Measured by ICP after digesting the film with aqua regia; ^{b)} Determined by AFM measuring a statistically relevant number of particles or films.

commented below, the preferential facet orientation that is also a key for interpreting the photocatalytic activity, derives from the specific binding strength of these Ru facets with H₂ that is larger for the 101 facet and causes the re-structuring of the nascent NPs.

ICP analysis of the films upon dissolution of Ru NPs with aqua regia determines the Ru loading per surface area or total mass of the film. **Table 1** gathers the main analytical and characterization data of the films under study.

The oxidation state of Ru and its strong interaction with the graphene layers was determined by analysis of the XPS. **Figure 1** shows the high-resolution C1s+Ru3d peaks recorded for both $\overline{Ru}(002)/G$ and $\overline{Ru}(002-101)/G$ films. The overlap between the C1s and Ru3d_{3/2} signals at about 284 eV does not allow determining the different types of C atoms and their percentage. However, the Ru electronic state in $\overline{Ru}(002)/G$ was established by analysis of the Ru3d_{5/2} peak at 280.11 eV that indicates only a single component corresponding to Ru(0).^[43]

The XPS analysis of $\overline{Ru}(002-101)/G$ film is similar to that of $\overline{Ru}(002)/G$. However, one difference observed for $\overline{Ru}(002-101)/G$ film was that the surface atomic proportion of Ru is about twice as higher as the one measured for $\overline{Ru}(002)/G$. Since the height of Ru NPs in $\overline{Ru}(002-101)/G$ is about double than that of $\overline{Ru}(002)/G$ (see Table 1) and typical penetration in XPS about 5 nm,^[44] less carbon and oxygen atoms are probed on the surface, explaining the increased surface atomic proportion of Ru atoms for films of similar Ru loading.

The defective nature of the graphene film and its multi-layer stacking was determined by Raman spectroscopy of the films. **Figure 2(a)** shows a representative Raman spectrum corresponding to $\overline{Ru}(002)/G$. As it can be seen there, the presence of the 2D, G, and D peaks appearing at 2800, as a broad-band, 1600 and 1354 cm⁻¹ was observed. The relative intensity of the G versus the D band in both Ru-containing films was about 1.04 that is in the range of the I_G/I_D ratios previously

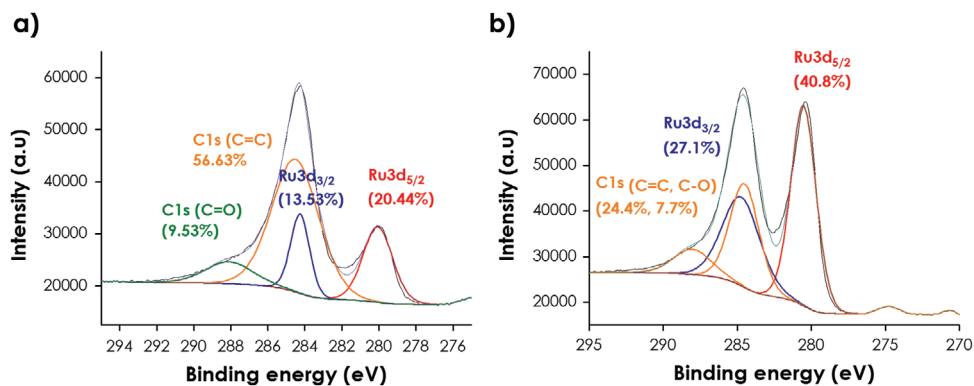


Figure 1. High-resolution XPS C1s and Ru3d_{3/2} peaks and their best deconvolution to individual components in the proportions indicated in the plot for a) Ru(002)/G and b) Ru(002-101)/G films.

reported for defective graphenes.^[45] A relatively intense peak at 440 cm⁻¹ attributable to the quartz substrate accompanied by other less intense peaks are recorded in the low-frequency range.^[46] No peaks corresponding to RuO₂ or other Ru oxide (528 cm⁻¹ strong, 646 cm⁻¹ medium intensity, and 716 cm⁻¹ weak)^[47,48] could be detected in the lower energy region of the Raman spectra. This failure to observe Ru oxides is in agreement with the XPS data in which the Ru oxidation state corresponds to Ru(0). Similar features were recorded for Ru(002-101)/G (Figure 2(b)), except that the signal-to-noise ratio was higher. Since Raman spectroscopy derives from scattered light the higher signal-to-noise ratio could probably be due to the different morphology and higher height Ru(002-101) NPs supported on G.

The prevalent metallic state of Ru NPs and their preferential crystallographic orientation were clearly determined by XRD for samples of higher Ru loading. Figure 3 shows the corresponding XRD patterns for the two Ru-containing graphene films under study with sufficiently high Ru loading (9.3 μg/cm², average lateral particle size 70 nm by FSEM). For other films with lower Ru content as those indicated in Table 1, no XRD peaks attributable to Ru could be recorded. These XRD patterns for films with high Ru loading are characterized by a broad diffraction band at 2θ value of 24° corresponding to the stacking of the graphene layers. In addition, one or two sharp peaks at 2θ values of 42° or 42° and 44° corresponding to the 002 or the 002 and 101 diffraction facets of metallic Ru NPs, respectively, were also recorded in Ru(002)/G and Ru(002-101)/G. For the sake of comparison, Figure S1, Supporting

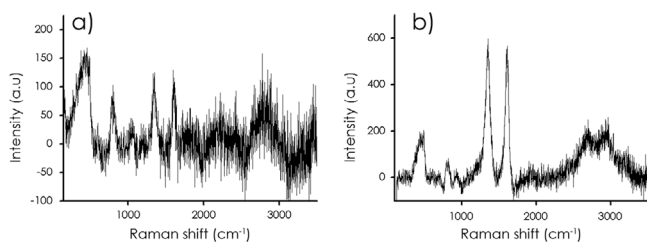


Figure 2. Raman spectra upon 514 nm excitation recorded for a) Ru(002)/G and b) Ru(002-101)/G films. The peak at 440 cm⁻¹ corresponds to the quartz substrate in agreement with the literature.^[46] Note that the signal-to-noise ratio reflects the nanometric thickness of the graphene films.

Information, shows also the XRD pattern of Ru NPs lacking any preferential orientation, in which the presence of a series of diffraction peaks corresponding to the various possible crystallographic planes can be observed. Therefore, XRD provides a firm evidence of the preferential facet orientation of Ru NPs in the Ru(002)/G and Ru(002-101)/G films.

As commented earlier, there are precedents in the literature showing that pyrolysis of natural polysaccharides containing metal precursors gives rise to metal NPs with preferential crystallographic orientation.^[36,37] One notable difference of the present samples with the existing precedents is that it is possible to obtain two different Ru nanocrystals by performing the pyrolysis in the absence (002 facet) or in the presence of H₂ (002 and 101 facets). Therefore, the results obtained disclose a reliable procedure to grow Ru crystals with one or two developed facets. Regarding the influence of H₂ on the Ru NP growth, it is proposed that under pyrolysis conditions the stronger H₂ binding and Ru hydride stability for the 101 plane in comparison to the 002 facet cause reorganization of the Ru NPs as they grow, favoring the appearance of the 101 facet in comparison with the thermodynamically more stable 002 plane. In the absence of H₂, under Ar atmosphere, the thermodynamically more stable 002 facet of Ru prevails. Similar proposals have been made earlier in the literature to explain changes in Ru clusters by interaction with H₂.^[49] This proposal is based on the theoretical calculations on models that will be commented below.

The thickness of the Ru(002)/G films and the morphology of the Ru NPs were studied by AFM. This technique with subnanometric vertical resolution indicates that the thickness of the graphene films was between 5 to 20 nm. Table 1 includes the exact thickness value for the samples under study. Frontal views of these films by AFM show the presence of Ru NPs adhered

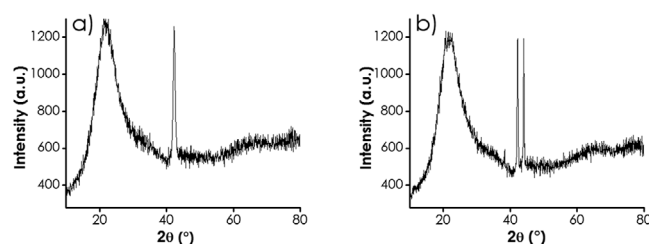


Figure 3. XRD patterns of a) Ru(002)/G and b) Ru(002-101)/G films.

to the graphene. **Figure 4** presents selected AFM images and representative height profiles for films thickness of the samples used as photocatalysts. These measurements were also employed to characterize Ru NPs and to understand better the reasons for the development of the 101 facet. Measurements on a statistically relevant number of Ru NPs for the $\overline{Ru}(002)/G$ film (see insets of Figure 4a,b for the number of particles) indicate that the average height was about 4.3 nm. Although the lateral size cannot be measured with accuracy by AFM due to the width of the probe tip, the morphology of Ru NPs appears as thin platelets

where the largest surface should correspond according to the XRD pattern to the 002 plane. This platelet morphology was later confirmed by high-resolution transmission electron microscopy (TEM). In the case of $\overline{Ru}(002-101)/G$ films, the average Ru NP height measured with subnanometric resolution was higher than that of $\overline{Ru}(002)/G$, about 7.6 nm, while the lateral size was estimated in the same range for $\overline{Ru}(002)/G$ and $\overline{Ru}(002-101)/G$ films. In other words, it seems that the experimental data indicate that the Ru NPs in the $\overline{Ru}(002-101)/G$ sample have the same basal area, but are taller than those of $\overline{Ru}(002)/G$.

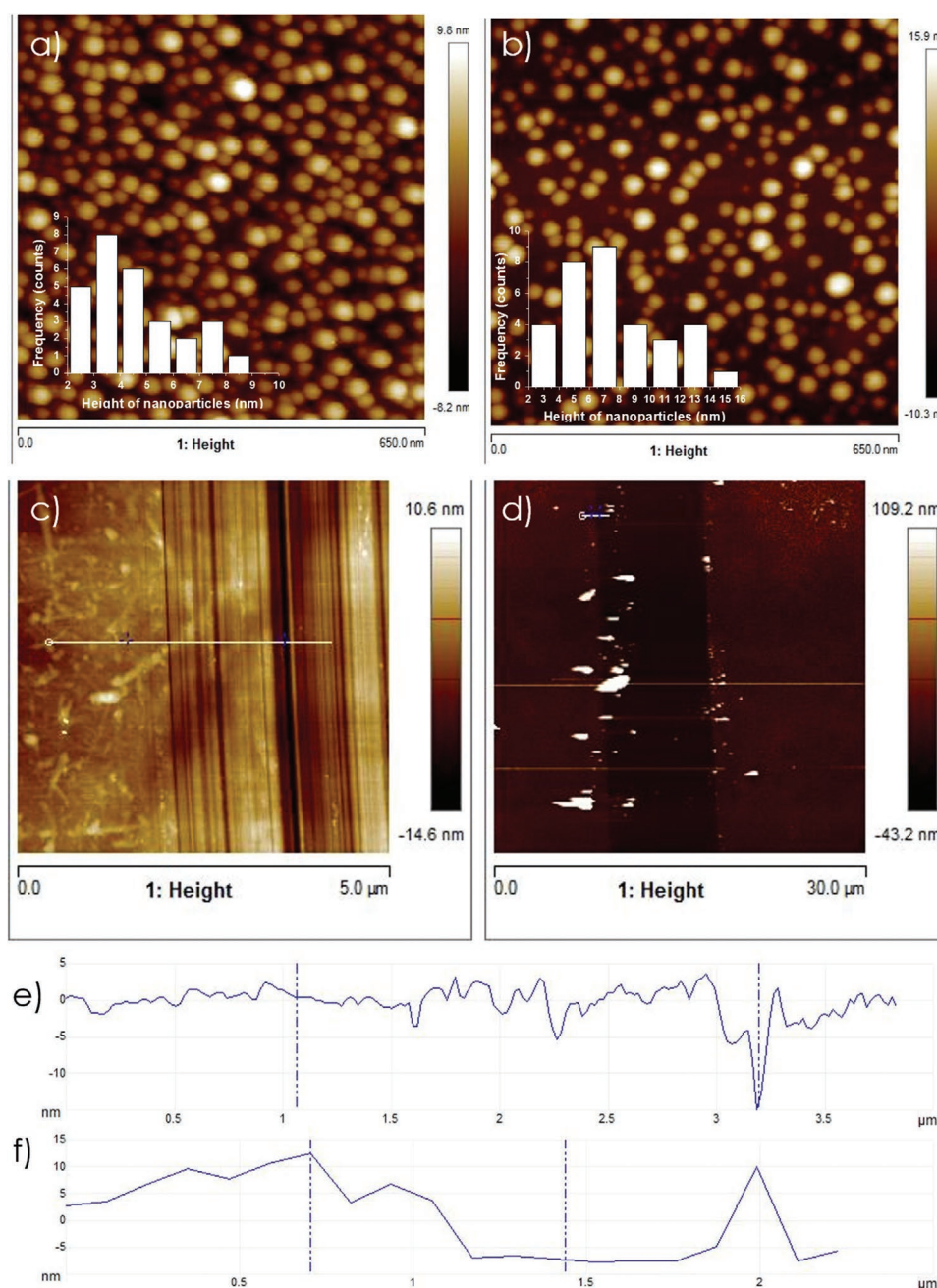
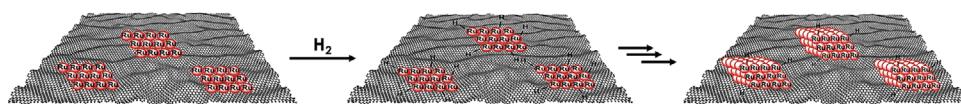


Figure 4. Frontal views of a) $\overline{Ru}(002)/G$ and b) $\overline{Ru}(002-101)/G$ showing the presence of Ru NPs on a continuous G film. The insets in frames (a) and (b) correspond to the histograms of Ru NP height. Bottom frames: G film thickness for $\overline{Ru}(002)/G$ (top) and $\overline{Ru}(002-101)/G$ (bottom) determined from the profiles along the white lines in the left images.



Scheme 2. Pictorial illustration of the growth of the 002 plane in $\overline{Ru}(002)/G$ and development of the 101 plane in $\overline{Ru}(002-101)/G$ when the pyrolysis is performed in the presence of H_2 .

It is proposed that the 002 plane grows parallel to the G plane, while the 101 facet determines the height of the Ru NPs. **Scheme 2** illustrates our proposal to rationalize the preferential orientation of Ru NPs in the two samples under study.

The preferential facet orientation determined by XRD at macroscopic scale was further confirmed by high-resolution TEM images by measuring the corresponding interplanar distances of individual NP after scratching a bit of the film from the quartz support. **Figure 5** shows two representative images taken for these two $\overline{Ru}(002)/G$ and $\overline{Ru}(002-101)/G$ films. Thus, for the lattice fringes of $\overline{Ru}(002-101)/G$ it was possible to measure two interplanar distances of 0.199 and 0.214 nm corresponding to the reported interplanar distance of the 101 and 002 facets of hexagonal Ru metal NPs (Figure 5a),^[50,51] while in the case of $\overline{Ru}(002)/G$ film a distance between planes of 0.214 nm, matching the expected value for the Ru 002 facet was measured (Figure 5b).

FESEM images of $\overline{Ru}(002)/G$ and $\overline{Ru}(002-101)/G$ films on quartz are shown in **Figure 6**. A clear dendritic patterning of the Ru NPs on G is observed for both films, revealing the non-homogeneous distribution of the NPs on the G film. This dendritic patterning probably arises from the agglomeration of atoms and clusters of Ru following a certain model on the G sheet and could be a direct consequence of the high temperature of the pyrolysis. $\overline{Ru}(002-101)/G$ displays a similar dendritic patterning and also a non-uniform distribution of Ru particles on the G sheets.

2.2. Photocatalytic Activity

Photoassisted CO_2 hydrogenation was performed in the gas phase by placing square $2 \times 2 \text{ cm}^2$ plates of $\overline{Ru}(002)/G$ or $\overline{Ru}(002-101)/G$ films on a sealed photoreactor that can be heated up to $150 \text{ }^\circ\text{C}$. Irradiation of the system was performed from the top with a collimated beam at a distance of 13 cm using the UV-vis output of a Xenon lamp.

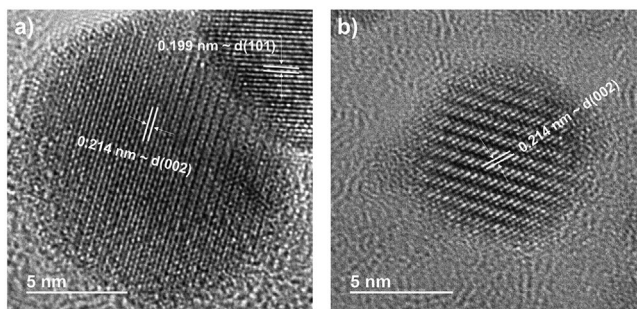


Figure 5. High-resolution TEM images of Ru NPs from a) $\overline{Ru}(002-101)/G$ and b) $\overline{Ru}(002)/G$ samples.

The only product detected in all of the photocatalytic experiments was CH_4 . Formation of other byproducts such as CO or higher hydrocarbons was undetectable (micro-GC detection limit $<0.1 \text{ } \mu\text{mol}$). The photocatalytic activity of the two nanometric thick films at $150 \text{ }^\circ\text{C}$ is displayed in **Figure 7** as mmols of CH_4 formed per mass of the film (Ru NPs and graphene) as a function of time. Supporting information provides details of how the mass of the $\overline{Ru}(002)/G$ film was determined. A previous control using a Ru-free G film did not exhibit measurable photocatalytic activity under these conditions, indicating that Ru NPs are necessary to observe the photoassisted methanation. If $\overline{Ru}(002)/G$ is irradiated at $150 \text{ }^\circ\text{C}$ in the absence of CO_2 or CO_2 is irradiated at $150 \text{ }^\circ\text{C}$ in the absence of any catalyst or if the photocatalyst and CO_2/H_2 mixture are not irradiated, formation of CH_4 was negligible (below 10 mmol g^{-1} at 24 h, compared to Figure 7), meaning that light, CO_2 and $\overline{Ru}(002)/G$ are necessary to observe CH_4 formation at this temperature. Similarly, another control at the same temperature with any of the two Ru-containing films, but in the dark, shows that the amount of CH_4 formed at this temperature is about one order of magnitude lesser. Since it is well known that Ru NPs are good catalysts for the thermo catalytic CO_2 hydrogenation at sufficiently high temperatures, the activity of $\overline{Ru}(002)/G$ in the dark was also tested at temperatures above $150 \text{ }^\circ\text{C}$. Important to be noted is that at temperatures of $200 \text{ }^\circ\text{C}$, catalytic methanation in the dark was significantly higher than at $150 \text{ }^\circ\text{C}$, but the contribution of dark catalytic methanation at $150 \text{ }^\circ\text{C}$ is less than 10% of the total CH_4 formed in the photocatalytic reaction. Performing photoassisted experiments at $150 \text{ }^\circ\text{C}$ ensures that the contribution of the thermo catalytic process is not relevant. Obviously, thermal production of CH_4 by $\overline{Ru}(002)/G$ would increase at higher temperatures, but the influence of the temperature on the dark thermal reaction was not further studied. In addition, keeping the temperature constant at $150 \text{ }^\circ\text{C}$, the CH_4 production rate increases with the light intensity in the range from 40 to 100 mW x cm^{-2} as measured with a calibrated photodiode (see Figure S2, Supporting Information), indicating that the process is assisted by light.

Figure 7 shows that although the amount of Ru in the two Ru-containing films is similar (see Table 1), the photocatalytic activity of $\overline{Ru}(002)/G$ film is significantly higher than

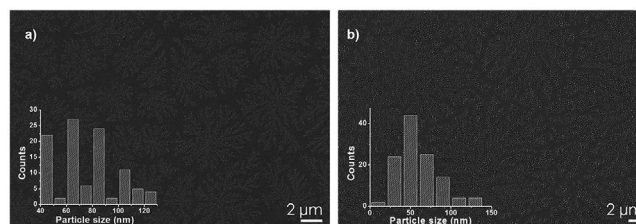


Figure 6. FESEM images of a) $\overline{Ru}(002)/G$ and b) $\overline{Ru}(002-101)/G$ on quartz showing the dendritic particle distribution.

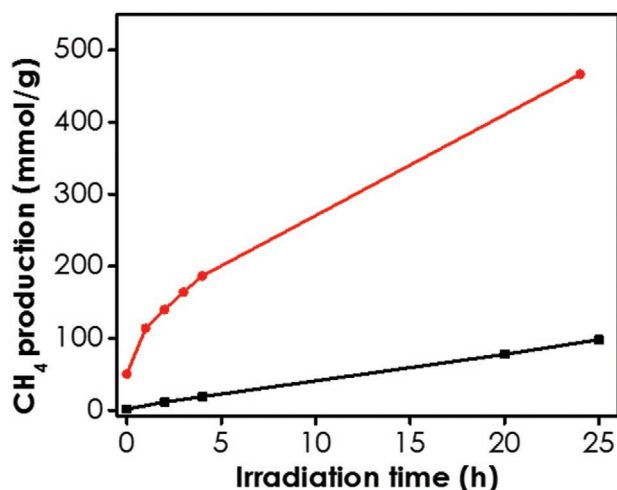


Figure 7. CH₄ temporal profile (mmol_{CH₄}/g_{catalyst}) at 150 °C under UV–vis irradiation measured for the two Ru-containing films presenting different preferential crystallographic orientations (■: Ru(002-101)/G and ●: Ru(002)/G). Reaction conditions: 1 quartz plate of 2 × 2 cm² as photocatalyst; P_{H₂} = 1.05 bar, P_{CO₂} = 0.25 bar.

that of Ru(002-101)/G analog. Ru NPs in which the 101 plane is observed in XRD exhibits less than one order of magnitude lower initial reaction rate and about eight times lower CH₄ production at final reaction time. Figure 7 shows that an initial reaction rate of 113.9 mmol of CH₄ / g of photocatalyst × h⁻¹ is reached in the first hour of irradiation at 150 °C for Ru(002)/G. This photocatalytic rate is remarkable and among the highest ever reported for the light-assisted Sabatier methanation. Table S1, Supporting Information, provides a comparison with other reported data. Although there are in the literature at least three reports with a high CH₄ methane production rate than the value achieved for Ru(002)/G herein, these higher rates were reported at higher temperatures (case of NiO/Ni-G) or with much higher light intensity corresponding to 10 Suns (case of Ru NPs supported on few layer double hydroxide) or 300 W Xe lamp (Ru/Al₂O₃). Under the mild conditions corresponding to the experiments reported in Figure 7, Ru(002)/G was the most active material.

Worth to remind is that this remarkable photocatalytic activity is produced by a nanometer-thin film. The total CH₄ production using Ru(002)/G as photocatalyst at 25 h was 7.5 times higher than the total C amount present in the film, indicating again the G film cannot be the origin of CH₄. Comparison of the activity data of Ru(002)/G or Ru(002-101)/G films indicate that the facet displaying the highest photocatalytic activity is the 002 facet.

As commented earlier when referring to the control experiments, the temperature exerts a considerable influence on the occurrence of dark versus photocatalytic methanation. The reaction temperature also plays a remarkable influence on the photocatalytic activity of Ru(002)/G. This influence was determined by carrying out the photoassisted CO₂ methanation at three different temperatures from 100 to 150 °C. The results are presented in Figure 8. From this Figure, a minor increase in photocatalytic activity occurs upon increasing the temperature from 100 to 120 °C. In contrast, when

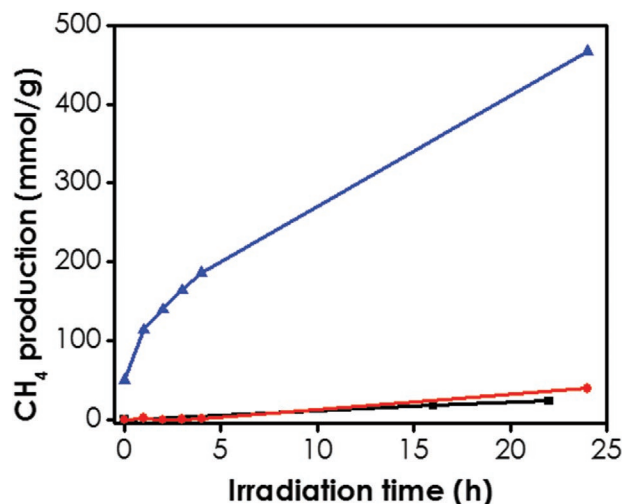


Figure 8. Time-CH₄ production (mmol g⁻¹) plot under illumination with a 150 W xenon lamp of a Ru(002)/G film at 100 (■), 120 (●), and 150 °C (▲). Reaction conditions: 1 quartz plate of 2 × 2 cm² (15.2 μg) as photocatalyst; P_{H₂} = 1.05 bar, P_{CO₂} = 0.25 bar.

performing the reaction at 150 °C, CH₄ production was notably increased reaching a rate of 113.9 mmol × h⁻¹ × g⁻¹ compared to 1.90 mmol × h⁻¹ × g⁻¹ obtained at 120 °C. By applying Arrhenius equation, an apparent activation energy for the photocatalytic methanation in this range of temperatures of 30.44 kcal × mol⁻¹ was determined.

The photoresponse of Ru(002)/G was determined by performing analogous photocatalytic methanation using passband (UV) and cut off (visible, λ > 450 nm) filters to ensure selective irradiation with UV or visible light. The results are shown in Figure 9. It should be noted that although the light power in these regions is different, the results provide firm evidence that

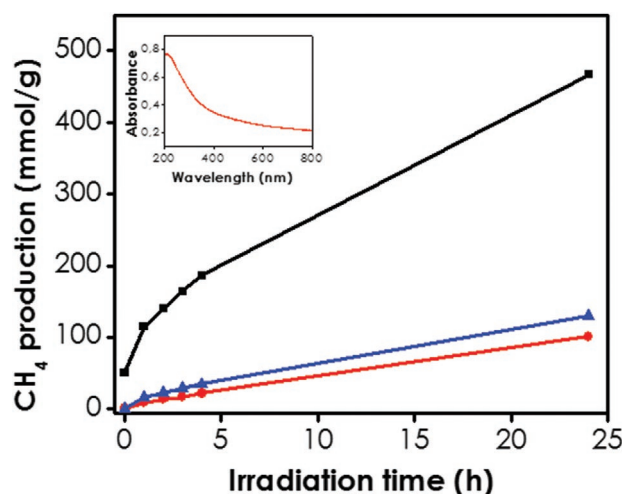


Figure 9. Time-CH₄ production (mmol g⁻¹) plot at 150 °C upon illumination by the output beam of a 150 W xenon lamp of Ru(002)/G film using different cut off filters (■: no filter, ●: pass band filter of 340 till 380 nm and ▲: cut-off filter for λ > 450 nm). The inset shows the UV–vis spectrum of Ru(002)/G film that is also very similar to that of Ru(002-101)/G. Reaction conditions: 1 quartz plate of 2 × 2 cm² (15.2 μg) as photocatalyst; P_{H₂} = 1.05 bar, P_{CO₂} = 0.25 bar.

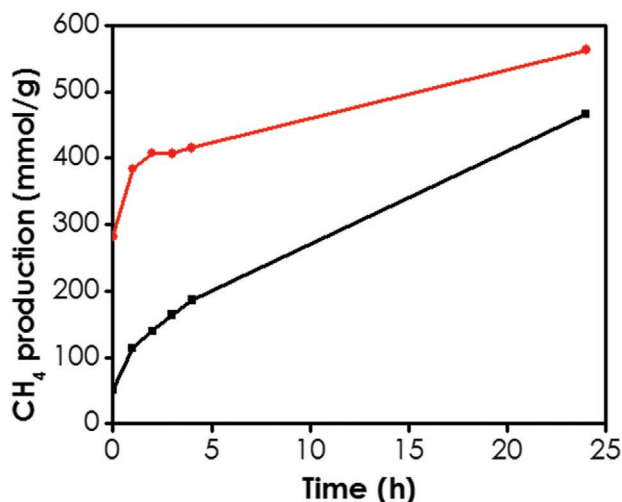


Figure 10. Time-CH₄ formation (mmol g⁻¹) plot of the photocatalytic CO₂ methanation in the presence of Ru(002)/G at 150 °C under irradiation from a 150 W xenon lamp in presence of 0.16 mmol of N,N-dimethylaniline (●) or H₂ (■, P_{H₂} = 1.05 bar). Reactions conditions: 1 quartz plate of 2 × 2 cm² as photocatalyst (15.2 μg); P_{CO₂} = 0.25 bar. Either N,N-dimethylaniline or H₂ as electron donor.

Ru(002)/G exhibits photoresponse all over the UV–vis wavelength range, what is in agreement with the optical absorption spectrum of the sample as shown in Figure 9 inset (for the UV–vis spectrum of Ru(002-101)/G see Figure S3, Supporting Information).

One important point is to determine the type of photocatalytic mechanism. Previous reports in the literature have revealed two general mechanisms, either photothermal^[9] or photoinduced charge separation.^[52] In the photothermal methanation, the photon energy is converted at the metal NP in local heat, increasing the temperature at the NP. In the photoinduced charge separation, conduction band electrons and valence band holes are generated promoting CO₂ reduction and H₂ oxidation, respectively. To address the reaction mechanism, the photoassisted CO₂ methanation was carried out in the absence of H₂, but in presence of dimethylaniline as electron donor. N,N-dimethylaniline radical cation typically undergoes dimerization to tetramethylbenzidine that does not interfere with the products in the gas phase.^[53] It is observed in Figure 10 that the addition of N,N-dimethylaniline in the absence of H₂ in the gas phase increases the rate of CH₄ formation by a factor of three reaching a value of 383.8 mmol_{CH₄} × g_{photocatalyst}⁻¹ × h⁻¹. This enhancement on the rate of CH₄ formation by replacing H₂ by N,N-dimethylaniline supports the photogeneration of electrons and holes on Ru(002)/G film as the most likely reaction mechanism.

This enhanced CH₄ production rate is in agreement with the better ability of N,N-dimethylaniline to act as electron donors

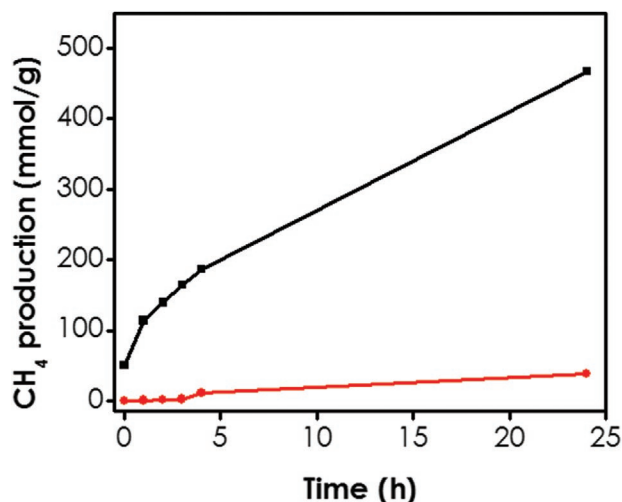
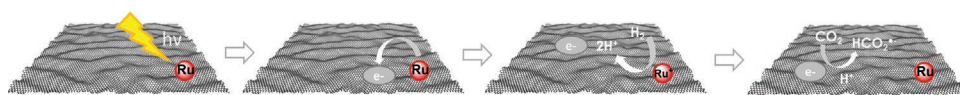


Figure 11. Comparison of the time-CH₄ (mmol g⁻¹) plot upon contacting Ru(002)/G at 150 °C under irradiation with a mixture of H₂ (1.05 bar) and CO₂ (0.25 bar) (■) and a second experiment in which Ru(002)/G was irradiated first with an H₂ atmosphere for 4 h and subsequent H₂ was removed and CO₂ added and the reaction continued in the dark (●). Reactions conditions: 1 quartz plate of 2 × 2 cm² as photocatalyst (15.2 μg); P_{H₂} = 1.05 bar of the first step, P_{CO₂} = 0.25 bar of the second step, irradiation with a 150 W Xe lamp.

compared to H₂, due to its lower oxidation potential. In the experiment with N,N-dimethylaniline, this aromatic compound acts simultaneously as a proton donor after the generation of the corresponding radical cation as indicated in Scheme 3. According to this mechanism, the role of graphene is to enhance electron/hole separation by accepting electrons. The high CH₄ production rates would be, then, a reflection of the efficient Ru NP-graphene heterojunction derived from the pyrolytic preparation procedure that ensures a strong grafting of the Ru NP on the graphene. However, the fact that photocatalytic CO₂ reduction occurs does not exclude the possibility of a certain contribution of the photothermal pathway.

As indicated in Scheme 3, a plausible mechanism after the photocatalytic event involves the intermediacy of ruthenium hydrides as intermediates of the methanation. This proposal is compatible with the well-known Ru hydride chemistry.^[54] To provide some support to this proposal, an additional experiment was performed in which first the photocatalyst was submitted to irradiation for 4 h in the presence of H₂, but in the absence of CO₂. Subsequently, in a second step and after complete evacuation of H₂, the pretreated Ru(002)/G film was exposed to CO₂ at 150 °C in the dark. The results are presented in Figure 11. If Ru–H species are formed in the step of photocatalytic irradiation, these intermediates should persist sufficiently long to attack CO₂ in the dark at 150 °C when this gas is admitted in the second step. The results obtained showed



Scheme 3. Proposal of the photocatalytic Sabatier CO₂ methanation mechanism. Upon light absorption by the Ru NPs, hot electrons migrate to the defective graphene sheet reaching a charge-separated state. Holes at Ru NPs oxidize H₂ to protons, while electrons and protons reduce CO₂.

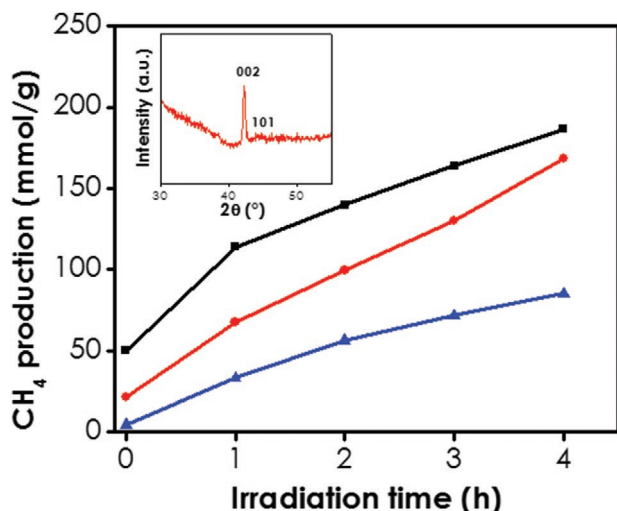


Figure 12. Temporal evolution of CH_4 production (mmol g^{-1}) upon consecutive reuse of the same $\overline{\text{Ru}}(002)/\text{G}$ film (■: 1st reuse, ●: 2nd reuse, and ▲: 3rd reuse). Inset: XRD pattern of three times used $\overline{\text{Ru}}(002)/\text{G}$ film indicating the diffraction peaks corresponding to Ru NPs. Reaction conditions: 1 quartz plate of $2 \times 2 \text{ cm}^2$ as photocatalyst ($15.2 \mu\text{g}$); $P_{\text{H}_2} = 1.05 \text{ bar}$, $P_{\text{CO}_2} = 0.25 \text{ bar}$, $150 \text{ }^\circ\text{C}$, 150 W Xe lamp .

that after contacting separately H_2 and CO_2 with the $\overline{\text{Ru}}(002)/\text{G}$ film, formation of CH_4 is detected, thus lending support to the intermediacy of some Ru-H as intermediate. Note that a control experiment in which the hydrogenation step is performed at $150 \text{ }^\circ\text{C}$ in the dark for 14 h, prior to H_2 outgassing and subsequent addition of CO_2 while the system is being irradiated at $150 \text{ }^\circ\text{C}$, only leads to the detection of minute amounts of CH_4 . This suggests that the formation of Ru-H at this temperature is a step being assisted by light. In this way, it is proposed that photogenerated electrons will form a Ru-H .

Photocatalyst stability was tested by performing three consecutive uses of the same $\overline{\text{Ru}}(002)/\text{G}$ film. The temporal CH_4 evolution of these stability tests is presented in **Figure 12**. As it can be seen there, significant deactivation is observed upon second reuse reflected by a decrease of the initial CH_4 formation rate (from 113.9 to $67.6 \text{ mmol} \times \text{g}^{-1} \times \text{h}^{-1}$) and CH_4 amount at final time. A third use results in a further decrease of the initial reaction rate and final CH_4 production. To better understand the origin of this deactivation, XRD pattern of the three-times used $\overline{\text{Ru}}(002)/\text{G}$ film was recorded and compared to that of the fresh sample. The corresponding diffractogram is presented also in

Figure 12 as an inset. Emergence of the peak at a 2θ value of 44° corresponding to the (101) facet was observed. Since the photocatalytic activity of the $\overline{\text{Ru}}(002-101)/\text{G}$ film is lower than that of $\overline{\text{Ru}}(002)/\text{G}$, it seems that under the reaction conditions exposure to H_2 at $150 \text{ }^\circ\text{C}$ under light irradiation causes reconstruction of Ru NPs, with the growth of the 101 facet. This would result in a worsened photocatalytic activity. Reconstruction of Ru NPs under reaction conditions has been previously reported^[55] in the literature and this will result in an irreversible decrease in photocatalytic activity from that of $\overline{\text{Ru}}(002)/\text{G}$ to the activity of Ru NPs having 101 facet, like $\overline{\text{Ru}}(002-101)/\text{G}$, as reflected in **Figure 7**.

2.3. Theoretical Calculations

In order to give some insight into the preferential $\text{Ru}(002)$ facet growth (**Figure 1a**) and the role of hydrogen developing the 101 plane, a computational approach was applied. Initial calculations with a Ru_{18} cluster model confirm that the (002) facet was thermodynamically more stable than the (101) by 1.46 eV and the expected ratio of the (002) versus the (101) facet should be 4.7 , in good agreement with the characterization data for $\overline{\text{Ru}}(002)/\text{G}$. This higher thermodynamic stability explains why under inert atmosphere the 002 facet is preferentially developed. The optimized cell unit ($2.67 \times 2.67 \text{ \AA}$) for the (002) facet was further characterized by electron localization function (**Figure 13b**) revealing a covalent bonding between Ru atoms. This fact indicates that the small model is suitable for studying the system as it reproduces the experimental atom distances and coordinates. For the calculations of adsorption on Ru, a capped model was used to obtain the MEP surface. This surface suggests a relatively positive region presenting a $V_{s,\text{max}}$ value of 24 kcal mol^{-1} .

A model containing a Ru_{12} cluster deposited on an aromatic surface ($1.14 \times 1.14 \text{ nm}$) mimicking the graphene layer was employed to estimate the activation of H_2 . In this model corresponding to the Ru NPs interacting with the graphene sheet, molecular hydrogen undergoes a dissociative adsorption ($E_{\text{dis}} = -1.4 \text{ eV}$) on the peripheral Ru atoms at the cluster/aromatic interface. The calculated H-H distance of the adsorbed H atoms was increased up to 2.29 \AA , thus confirming their spontaneous dissociation (**Figure 14**). In addition, both hydrogen atoms have a similar Ru-H distance ($d_{\text{Ru-H}}$ of 1.72 and 1.74 \AA , respectively). These values indicate that it is not the spontaneous H_2 dissociation, but the subsequent CO_2 attack by

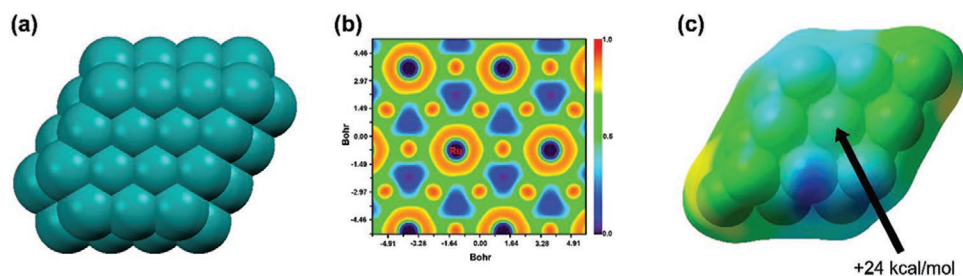


Figure 13. a) Crystallographic disposition of Ru (002) plane along the c axis; b) Electron localization function (ELF, XY plane) for optimized $\text{Ru}(002)$ cell unit, and c) MEP surface (plotted at 0.002 a.u.) for a Ru_{18} model cluster.

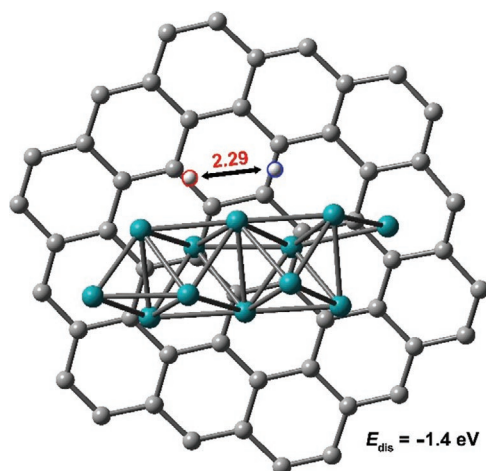


Figure 14. Dissociative adsorption on the Ru-graphene interface at PBE-D3/def2SVP level of theory. The corresponding hydrogen atoms are highlighted in blue and red colours. Hydrogen of aromatic surface has been omitted for clarity.

photogenerated electrons coupled with proton transfer the rate-determining step in the photocatalytic CO₂ reduction.

3. Conclusion

Pyrolysis of alginate films containing a Ru salt leads to the formation of films of defective G containing Ru NPs with preferential 002 facet orientation. The presence of H₂ during the pyrolysis promotes the growth of Ru NPs with 002 and 101 planes. Theoretical studies suggest that the stronger interaction of the 002 facet of Ru with graphene together with the higher H₂ adsorption energy onto the 101 facet compared to the 002 plane are the factor responsible for this unique control of the Ru crystal morphology. The films of oriented Ru NPs grafted on defective graphene exhibit a remarkable activity to promote the photocatalytic CO₂ methanation through a mechanism involving charge separation, reaching a CH₄ production rate at 150 °C over 110 mmol CH₄ x g_{photocatalyst}⁻¹ x h⁻¹ that is among the highest ever reported, probably reflecting the efficient Ru NP-graphene heterojunction due to the strong grafting of Ru on graphene as a consequence of the pyrolytic preparation method. Overall the present study shows the vast potential of defective graphene films of nanometric dimensions to form efficient heterojunctions with enhanced activity as photocatalyst with potential application in related CO₂ reduction reactions using H₂O as electron and proton source.

4. Experimental Section

Preparation of Ru(002)/G: Alginate acid from Sigma-Aldrich (Lot #SLBL2988V) was first dispersed in 9 mL of MilliQ water under magnetic stirring followed by the addition of 1 mL of aqueous NH₄OH solution (25%) to ensure its complete dissolution. After stirring for 2 h, the resulting solution of ammonium alginate was filtered through a syringe of 0.45 μm pore diameter to remove eventual impurities present in the powder. 148 mg of hexaammineruthenium(III) chloride purchased from Sigma-Aldrich (Lot#MKCF0161) was dissolved in 200 μL of MilliQ

water. 3 mL of filtered ammonium alginate solution was, then, added to the ruthenium complex solution and the mixture was left under stirring for 3 h. The resulting suspension was then filtered through a syringe of 0.45 μm diameter. The films were prepared by casting the solution on a freshly cleaned quartz plate (1x1 cm²) at 4000 rpm for 30 s. The films were dried at 60 °C for 1 h prior to submitting them to pyrolysis under Ar atmosphere at a heating rate of 5 °C min⁻¹ up to 1000 °C and a dwelling time of 1 h at the final temperature. The plates were allowed to cool at room temperature under Ar atmosphere. The amount of Ru was determined by ICP-OES by immersing the plates into aqua regia for 24 h and analyzing the Ru content of the resulting solution.

Preparation of Ru(002-101)/G: Alginate acid purchased from Sigma-Aldrich (Lot #SLBL2988V) was first dispersed in 9 mL of MilliQ water followed by the addition of 1 mL of aqueous NH₄OH solution (25%) to ensure its complete dissolution. After stirring for 2 h, the resulting solution of ammonium alginate was filtered through a syringe with a Nylon filter of 0.45 μm pore diameter to remove eventual impurities present in the powder. 148 mg of hexaammineruthenium (III) chloride purchased from Sigma-Aldrich (Lot#MKCF0161) was separately dissolved in 200 μL of MilliQ water. 3 mL of the filtered ammonium alginate solution was added to the metallic solution and the resulting mixture was left under stirring for 3 h. The color of the resulting suspension turned dark brown. The resulting suspension was then filtered through a syringe of 0.45 μm diameter. The films were prepared by casting the solution on a freshly cleaned quartz plate (1x1 cm²) at 4000 rpm for 30 s. The films were dried for 1 h at 60 °C prior to pyrolysis under 5% H₂/ 95% Ar atmosphere at a heating rate of 5 °C min⁻¹ up to 1000 °C and dwelling time of 1 h at the final temperature. The amount of Ru was determined by ICP-OES analysis by immersing the plates into aqua regia for 24 h and analyzing the Ru content of the resulting solution.

Determination of the Amount of Catalyst Deposited on the Quartz Substrate: The mass of the photocatalyst was determined using the following procedure: based on the amount of alginate acid precursor; the mass of an aqueous solution of ammonium alginate (8 wt.%) deposited onto a quartz substrate by spin coating was determined with a balance of 0.1 mg nominal precision by the difference between the quartz substrate with and without the solution film. Thermogravimetric analysis shows that during the pyrolysis process at 1000 °C a mass reduction of 76.5% occurs while alginate acid was graphitized. Knowing the mass of solution deposited onto a 2x2cm² quartz substrate, the ammonium alginate content (8 wt.%), and the mass reduction in the pyrolysis, the weight of the residual graphene can be estimated by applying the equation 0.08x0.76 x mass of the solution. In this way, most of the experiments were performed with films containing an estimated mass of 15.2 μg of graphene in 2x2 cm² films.

Photocatalytic Reactions: The photocatalytic activity of the materials was evaluated using a photoreactor consisting of a homemade stain steel body with a top quartz window with a truncated conical shape. The total capacity of the photoreactor was 40 mL. The temperature and pressure inside the photoreactor were measured by an internal thermocouple and a manometer, respectively. The photoreactor was located 3 cm below the Xe lamp. The temperature of the H₂ and CO₂ gas mixture was 150 °C unless stated otherwise. For each measurement 1 plate of 2x2 cm² of the photocatalyst was used. H₂ and CO₂ were introduced in a 4:1 molar ratio up to achieve a final pressure of 1.3 bar. The photoreactor was heated at the desired temperature prior to irradiation and once the temperature was stabilized, the photocatalyst was irradiated from the top through fiber optics with UV-vis light from a 150 W Xe lamp. The evolved CH₄ was analyzed using a gas chromatograph (Agilent 490 MicroGC) equipped with two channels, both with TC detectors and Ar as the carrier gas. Quantification of the percentage of each gas was based on prior calibration of the system by injecting mixtures with known percentages of gases.

Supporting Information

Supporting Information is available from the Wiley Online Library or from the author.

Acknowledgements

Support by the Ministerio de Ciencia e Innovación (Severo Ochoa and RTI2018-098237-B-C21) and Generalitat Valenciana (Prometeo 2017/083) was acknowledged. Thanks are due to Galicia Supercomputing Center. A.A. thanks UEMF (Euromed Unniversity Fes) and UPV for an Erasmus+ 2019-1-ES01-KA107-062073 Scholarship. A.P. thanks the Spanish Ministry for a Ramón y Cajal research associate contract.

Conflict of Interest

The authors declare no conflict of interest.

Data Availability Statement

The data that support the findings of this study are available from the corresponding author upon reasonable request.

Keywords

graphene films, oriented Ru nanoparticles, photo-assisted sabatier reaction, photocatalytic CO₂ hydrogenation, ruthenium nanoparticles, solar photocatalysis

Received: January 14, 2022

Revised: February 5, 2022

Published online: March 16, 2022

- [1] W. Steffen, K. Richardson, J. Rockström, S. E. Cornell, I. Fetzer, E. M. Bennett, R. Biggs, S. R. Carpenter, W. de Vries, C. A. de Wit, C. Folke, D. Gerten, J. Heinke, G. M. Mace, L. M. Persson, V. Ramanathan, B. Reyers, S. Sörlin, *Science* **2015**, 347, 1259855.
- [2] Z. Liu, K. Wang, Y. Chen, T. Tan, J. Nielsen, *Nat. Catal.* **2020**, 3, 274.
- [3] S. Sarp, S. G. Hernandez, C. Chen, S. W. Sheehan, *Joule* **2021**, 5, 59.
- [4] M. D. Porosoff, B. Yan, J. G. Chen, *Energy Environ. Sci.* **2016**, 9, 62.
- [5] S. Roy, A. Cherevotan, S. C. Peter, *ACS Energy Lett.* **2018**, 3, 1938.
- [6] J. Albero, Y. Peng, H. García, *ACS Catal.* **2020**, 10, 5734.
- [7] U. Ulmer, T. Dingle, P. N. Duchesne, R. H. Morris, A. Tavasoli, T. Wood, G. A. Ozin, *Nat. Commun.* **2019**, 10, 3169.
- [8] T. H. Tan, B. Xie, Y. H. Ng, S. F. B. Abdullah, H. Y. M. Tang, N. Bedford, R. A. Taylor, K.-F. Aguey-Zinsou, R. Amal, J. Scott, *Nat. Catal.* **2020**, 3, 1034.
- [9] M. Cai, Z. Wu, Z. Li, L. Wang, W. Sun, A. A. Tountas, C. Li, S. Wang, K. Feng, A.-B. Xu, *Nat. Energy* **2021**, 6, 807.
- [10] P. G. O'Brien, A. Sandhel, T. E. Wood, A. A. Jelle, L. B. Hoch, D. D. Perovic, C. A. Mims, G. A. Ozin, *Adv. Sci.* **2014**, 1, 1400001.
- [11] P. G. O'Brien, K. K. Ghuman, A. A. Jelle, A. Sandhel, T. E. Wood, J. Y. Y. Loh, J. Jia, D. Perovic, C. V. Singh, N. P. Kherani, C. A. Mims, G. A. Ozin, *Energy Environ. Sci.* **2018**, 11, 3443.
- [12] D. Mateo, J. Albero, H. García, *Joule* **2019**, 3, 1949.
- [13] P. Sharma, S. Kumar, O. Tomanec, M. Petr, J. Zhu Chen, J. T. Miller, R. S. Varma, M. B. Gawande, R. Zbořil, *Small* **2021**, 17, 2006478.
- [14] C. Wang, S. Fang, S. Xie, Y. Zheng, Y. H. Hu, *J. Mater. Chem. A* **2020**, 8, 7390.
- [15] J. Ren, S. Ouyang, H. Xu, X. Meng, T. Wang, D. Wang, J. Ye, *Adv. Energy Mater.* **2017**, 7, 1601657.
- [16] D. Mateo, J. Albero, H. García, *Energy Environ. Sci.* **2017**, 10, 2392.
- [17] D. Mateo, A. M. Asiri, J. Albero, H. García, *Photochem. Photobiol. Sci.* **2018**, 17, 829.
- [18] D. Mateo, J. Albero, H. García, *Appl. Catal., B* **2018**, 224, 563.
- [19] J. Barrio, D. Mateo, J. Albero, H. García, M. Shalom, *Adv. Energy Mater.* **2019**, 9, 1902738.
- [20] L. Liu, A. Corma, *Chem. Rev.* **2018**, 118, 4981.
- [21] K. Lee, M. Kim, H. Kim, *J. Mater. Chem.* **2010**, 20, 3791.
- [22] Q. Zhang, H. Wang, *ACS Catal.* **2014**, 4, 4027.
- [23] R. Qin, N. Zheng, *Chem Catal.* **2019**, 5, 1935.
- [24] T. Wang, S. Wang, Q. Luo, Y.-W. Li, J. Wang, M. Beller, H. Jiao, *J. Phys. Chem. C* **2014**, 118, 4181.
- [25] L. M. Falicov, G. A. Somorjai, *Proc. Natl. Acad. Sci. USA* **1985**, 82, 2207.
- [26] Y. Xia, Y. Xiong, B. Lim, S. E. Skrabalak, *Angew. Chem., Int. Ed.* **2009**, 48, 60.
- [27] K. Zhou, Y. Li, *Angew. Chem., Int. Ed.* **2012**, 51, 602.
- [28] Z. Peng, H. Yang, *Nano Today* **2009**, 4, 143.
- [29] E. Ramirez, L. Eradès, K. Philippot, P. Lecante, B. Chaudret, *Adv. Funct. Mater.* **2007**, 17, 2219.
- [30] Y.-K. Peng, Y. Hu, H.-L. Chou, Y. Fu, I. F. Teixeira, L. Zhang, H. He, S. C. E. Tsang, *Nat. Commun.* **2017**, 8, 675.
- [31] J. D. Hoefelmeyer, K. Niesz, G. A. Somorjai, T. D. Tilley, *Nano Lett.* **2005**, 5, 435.
- [32] P. R. Sajanlal, T. S. Sreepasad, A. K. Samal, T. Pradeep, *Nano Rev.* **2011**, 2, 5883.
- [33] H. G. Yang, C. H. Sun, S. Z. Qiao, J. Zou, G. Liu, S. C. Smith, H. M. Cheng, G. Q. Lu, *Nature* **2008**, 453, 638.
- [34] S. E. Habas, H. Lee, V. Radmilovic, G. A. Somorjai, P. Yang, *Nat. Mater.* **2007**, 6, 692.
- [35] F.-R. Fan, D.-Y. Liu, Y.-F. Wu, S. Duan, Z.-X. Xie, Z.-Y. Jiang, Z.-Q. Tian, *J. Am. Chem. Soc.* **2008**, 130, 6949.
- [36] A. Primo, I. Esteve-Adell, J. F. Blandez, A. Dhakshinamoorthy, M. Álvaro, N. Candu, S. M. Coman, V. I. Parvulescu, H. García, *Nat. Commun.* **2015**, 6, 8561.
- [37] A. Primo, I. Esteve-Adell, S. N. Coman, N. Candu, V. I. Parvulescu, H. Garcia, *Angew. Chem., Int. Ed.* **2016**, 55, 607.
- [38] D. Mateo, I. Esteve-Adell, J. Albero, J. F. S. Royo, A. Primo, H. Garcia, *Nat. Commun.* **2016**, 7, 11819.
- [39] S. Frindy, A. El Kadib, M. Lahcini, A. Primo, H. Garcia, *ACS Catal.* **2016**, 6, 3863.
- [40] I. Esteve-Adell, N. Bakker, A. Primo, E. Hensen, H. Garcia, *ACS Appl. Mater. Interfaces* **2016**, 8, 33690.
- [41] D. Mateo, I. Esteve-Adell, J. Albero, A. Primo, H. Garcia, *Appl. Catal., B* **2017**, 201, 582.
- [42] A. Dhakshinamoorthy, I. E. Adell, A. Primo, H. Garcia, *ACS Sustainable Chem. Eng.* **2017**, 5, 2400.
- [43] R. Pongilat, K. Nallathamby, *ACS Appl. Mater. Interfaces* **2018**, 10, 38853.
- [44] M. Benelmekki, A. Erbe, in *Chapter 1 - Nanostructured thin films—background, preparation and relation to the technological revolution of the 21st century*, Vol. 14, (Eds: M. Benelmekki, A. Erbe), Elsevier, **2019**, pp. 1–34.
- [45] J. He, A. Anouar, A. Primo, H. García, *Nanomaterials* **2019**, 9, 895.
- [46] M. Morana, B. Mihailova, R. J. Angel, M. Alvaro, *Phys. Chem. Miner.* **2020**, 47, 34.
- [47] S. Mar, C. Chen, Y. Huang, K.-K. Tiong, *Appl. Surf. Sci.* **1995**, 90, 497.
- [48] Q. Lu, Y. Guo, P. Mao, K. Liao, X. Zou, J. Dai, P. Tan, R. Ran, W. Zhou, M. Ni, *Energy Storage Mater.* **2020**, 32, 20.
- [49] L. Liu, M. Yu, B. Hou, Q. Wang, B. Zhu, L. Jia, D. Li, *Nanoscale* **2019**, 11, 8037.
- [50] T. W. Hansen, J. B. Wagner, P. L. Hansen, S. Dahl, H. Topsøe, C. J. H. Jacobsen, *Science* **2001**, 294, 1508.
- [51] B.-S. Lou, P. Veerakumar, S.-M. Chen, V. Veeramani, R. Madhu, S.-B. Liu, *Sci. Rep.* **2016**, 6, 19949.
- [52] F. Zhang, Y.-H. Li, M.-Y. Qi, Y. M. A. Yamada, M. Anpo, Z.-R. Tang, Y.-J. Xu, *Chem Catal.* **2021**, 1, 272.
- [53] M. Kirchgessner, K. Sreenath, K. R. Gopidas, *J. Org. Chem.* **2006**, 71, 9849.
- [54] J. García-Antón, M. R. Axet, S. Jansat, K. Philippot, B. Chaudret, T. Pery, G. Buntkowsky, H.-H. Limbach, *Angew. Chem., Int. Ed.* **2008**, 47, 2074.
- [55] D. Bumüller, A.-S. Hehn, E. Waldt, R. Ahlrichs, M. M. Kappes, D. Schooss, *J. Phys. Chem. C* **2017**, 121, 10645.